Detecting the surface composition of geological features on Europa and Ganymede using a surface dust analyzer

William Goode [a,*], Sascha Kempf [a], Jürgen Schmidt [b,c]

[a] *LASP, University of Colorado, Boulder, CO, USA*
[b] *Institute of Geological Sciences, Freie Universität, Berlin, Germany*
[c] *Space Physics and Astronomy Research Unit, University of Oulu, Finland*

ARTICLE INFO

ABSTRACT

Europa and Ganymede are both likely to have subsurface oceans (Carr et al., 1998; Khurana et al., 1998; Kivelson et al., 2000). Young surface features may provide an opportunity to sample material from either a subsurface ocean or bodies of liquid water near the surface (McCord et al., 1999, 2001). Detailed compositional information is of large interest for understanding the evolution, oceanic chemistry, and habitability of these moons. To develop an altitude-dependent model for the detectability of ejecta particle composition originating from surface features of a given size, we simulate detections by a dust analyzer with the capability of measuring compositional makeup on board a spacecraft performing close flybys of Europa and Ganymede (Postberg et al., 2011). We determine the origin of simulated detections of ejecta by backtracking their trajectories to the surface using velocity distributions given in the ejecta cloud model by Krivov et al. (2003). Our model is useful for designing flybys with typical closest approach altitudes, such as the ones planned for NASA's Europa Clipper mission, where we wish to accurately identify the composition of surface features using a dust analyzer.

1. Introduction

Jupiter's icy Galilean satellites, Europa, Ganymede, and Callisto, likely possess subsurface oceans (Carr et al., 1998; Khurana et al., 1998; Kivelson et al., 2000). While the terrain on Callisto is heavily cratered with little indication of recent geological activity (Schenk, 1995; Greeley et al., 2000), the surfaces of Europa and Ganymede are relatively young (Pappalardo et al., 1998; Cassen et al., 1980), with features bearing chemical traces of the oceans or bodies of liquid water below (McCord et al., 1999, 2001). Mapping hydrated minerals along with other trace compounds to features with morphologies that suggest exposed subsurface material, such as lineae and chaos regions on Europa (Pappalardo and Sullivan, 1996; O'Brien et al., 2002), can help distinguish endogenic from exogenic material. Therefore, to gain knowledge on the oceanic chemistry and habitability, it is very useful to acquire the composition of non-water-ice material directly from surface features, which undergo exchange processes between the ocean and surface.

A surface dust analyzer with the capability of measuring compositional makeup aboard a spacecraft performing close flybys of these moons acquires compositional information of surface ejecta released by interplanetary meteoroid bombardment. The concept of such a dust analyzer is given by Grün et al., 2002 (see also Postberg et al. (2011) and Kempf et al. (2014)). A dust analyzer detects individual particles as they impact the instrument target at hypervelocities (several km/s) and measures the ionic composition of the impact plasma plume via time-of-flight (TOF) mass spectroscopy. Laboratory experiments have shown how the particle's chemical composition, as well as that of the instrument target, influences the resulting impact plasma registered by a dust analyzer (Goldsworthy et al., 2003; Srama et al., 2004, 2009). While remote sensing typically shows the dominant chemical species at high spatial resolution on the surface, surface dust analyzers can detect chemical species, including organic compounds (Postberg et al., 2008, 2018; Srama et al., 2009) and sodium salts (Postberg et al., 2009), embedded in the ice at the ppm level providing "ground truth" for interpreting remote sensing data by acquiring in situ compositional data on material originating from the surface (Postberg et al., 2011). Analogous to photons for remote sensing, ejecta emitted from the surface carry chemical information regarding their place of origin (Grün et al., 2002).

The model for the ejecta cloud formation at the Galilean satellites is given in detail by Krivov et al. (2003). The dynamical phase space of particles in ejecta clouds surrounding Europa and Ganymede is used to associate particle detections and compositional information with likely

---

sources on the surface, namely a geological feature of interest. This model is the basis for detection statistics by a surface dust analyzer on a given flyby trajectory. To derive the characteristic chemical constituents of a surface feature, it is important to guide flyby design for acquiring an adequate series of compositional data that can be associated with the feature.

Given the stochastic nature of the impactor ejecta mechanism, we apply Monte Carlo (MC) simulations of detections acquired during close flybys to characterize the statistics of the detection time series over a feature showing which particles originate from the feature itself. This depends largely on the altitude of the flyby and the size of the feature.

This paper serves to demonstrate the implication of the ejecta cloud model on the capability of a dust analyzer to map the composition of geological features on the surfaces of the Europa and Ganymede. We use the Surface Dust Analyzer (SUDA) on NASA's Europa Clipper mission as the reference instrument (Kempf et al., 2014). A major science goal for SUDA is to identify the composition of material from young geological features of interest on Europa's surface. SUDA will be the first instrument to leverage the nature of an ejecta cloud to map surface composition. We first briefly review the ejecta cloud model in the next section.

2. Ejecta cloud model

Interplanetary micrometeoroids enter Jupiter's gravitational sphere of influence losing their directional characteristics, resulting in a nearly isotropic impactor flux onto the surface of the moon. Impacts with speeds of ~ 20 km/s at Europa and Ganymede release surface material with a total mass several thousand times that of the original impactor (Krivov et al., 2003; Koschny and Grün, 2001a). A fraction of the impactor's kinetic energy is distributed among a population of ejecta particles that are kicked up into Keplerian trajectories around the moon. The ejecta do not mutually collide and are not affected by drag or electromagnetic forces, due to their low charge to mass ratio (Horányi, 1996).

Data returned by the dust detector onboard the Galileo spacecraft confirms the presence of ejecta clouds surrounding Europa, Ganymede, and Callisto (Krüger et al., 2003; Sremčević et al., 2005). While multiple populations of impactors, including particles on bound orbits about Jupiter are present, interplanetary dust particles (IDPs) dominate the mass flux reaching these moons, which subsequently dominates the ejecta yield. Statistical analysis of the data by Sremčević et al. (2005) concludes that the population responsible for the ejecta clouds consists of IDPs with isotropically distributed velocities as well as retrograde orbits with respect to the Sun.

The details of the IDP model does not significantly affect the outcome of this study. The ejecta production depends linearly on the projectile impact rate. According to Grün et al. (1985), the mass flux of interplanetary projectiles strongly peaks at 100 μm IDPs. This has been used by Krivov et al. (2003) to estimate this projectile rate by taking the total mass flux assuming the IDP flux arrives entirely as 100 μm particles, which is a very reasonable assumption. This in turn implies that the relevant number is the total mass flux while the other aspects of the IDP model itself are not as relevant. This is shown to be consistent with the properties of the dust envelopes of the Galilean moons as they were measured with the Dust Detection Subsystem of the Galileo orbiter (Krüger et al., 2003; Sremčević et al., 2005). Therefore, we are going to use the same numbers in this paper, although upgrades of the Divine model have been suggested (Grün and Staubach, 1996) and alternative models have been proposed for inner (Dikarev et al., 2005a,b,c) and outer solar system (Poppe, 2016).

2.1. Interplanetary impactors

The mass distribution of interplanetary meteoroids is dominated by particles with mass 10^{-8} kg traveling at speeds, $v_{imp}^{\infty} = 9.0$ km/s relative to Jupiter prior to gravitational focusing (Grün et al., 1985; Divine, 1993;

Krivov et al., 2003).

Gravitational focusing by Jupiter leads to an enhancement in both the speed and number density of the impactor population at the Galilean moons (Colombo et al., 1966; Spahn et al., 2006b). The impactor speed enhancement is

$$\frac{v_{imp}}{v_{imp}^{\infty}} = \sqrt{1 + \frac{2GM_J}{r\left(v_{imp}^{\infty}\right)^2}},$$
(1)

where G is the gravitational constant, M_J is the mass of Jupiter, and r is the orbital distance of the observer relative to Jupiter. The number density of the interplanetary impactors is enhanced by

$$\frac{n_{imp}}{n_{imp}^{\infty}} = \frac{1}{2}\frac{v_{imp}}{v_{imp}^{\infty}} + \frac{1}{2}\sqrt{\left(\frac{v_{imp}}{v_{imp}^{\infty}}\right)^2 - \left(\frac{R_J}{r}\right)^2\left(1 + \frac{2GM_J}{R_J\left(v_{imp}^{\infty}\right)^2}\right)}$$
(2)

where R_J is the mean radius of Jupiter. This formulation was first derived by Colombo et al. (1966), with a typographical correction provided by Spahn et al. (2006b). With Eqs. (1) and (2), the mass flux of impactors as a function of distance from Jupiter is

$$F(r) = F_{imp}^{\infty}\frac{v_{imp}(r)}{v_{imp}^{\infty}}\frac{n_{imp}(r)}{n_{imp}^{\infty}},$$
(3)

where $F_{imp}^{\infty} = 7.6 \times 10^{-16}$ kg m^{-2} s^{-1} is the IDP flux at Jupiter's heliocentric distance (Divine, 1993).

2.2. Hypervelocity impacts on the moon's surface

Laboratory experiments have been conducted to study hypervelocity impacts on "dirty" ice with varying percentages of silicate contents, G_{sil}, by (Koschny and Grün, 2001a, and references therein). They used all available data to derive an empirical relation for the ejecta mass yield, m_e/m_{imp}

$$Y = 2.85 \times 10^{-8} \times 0.0149^{G_{sil}/100} \times \left(\frac{1 - G_{sil}/100}{927} + \frac{G_{sil}/100}{2800}\right)^{-1} \times m_{imp}^{0.23}v_{imp}^{2.46}$$
(4)

where m_{imp} and v_{imp} are the typical mass and velocity of the impactors (both in SI units). The total mass production rate from the surface is

$$M^+ = F_{imp}YS,$$
(5)

where $S = \pi R_m^2$ is the cross section of the moon. Overall, the ejecta production of the Galilean moons is due to a stationary flux and therefore is not time-dependent (Sremčević et al., 2003).

The mass distribution of the ejecta particles is well matched by a power law. This is supported by laboratory experiments of hypervelocity impacts onto icy targets (Koschny and Grün, 2001b, and references therein). The total number of ejecta lager than a given size ($>s$) released per unit time is

$$N^+(>s) = \frac{3 - \alpha}{\alpha}\frac{M^+}{m_{max}}\left(\frac{s_{max}}{s}\right)^{\alpha},$$
(6)

as given by Spahn et al. (2006a) (Note: They denote the slope with γ). We assume a slope, $\alpha = 12/5$ (Spahn et al., 2006a; Krivov et al., 2003), which is typical where cratering is the dominant process (Krivov et al., 2000, 2003). m_{max} and s_{max} are the maximum mass and size of the ejecta distribution and are taken to be that of the typical impactor, 10^{-8} kg and 10^{-4} m, respectively.

The initial speed distribution of the ejecta at the surface also follows a power law,

$$f_u = \frac{\gamma}{u_0}\left(\frac{u}{u_0}\right)^{-\gamma-1}\Theta[u - u_0] \tag{7}$$

(Spahn et al., 2006a), where u_0 is the lower bound of the distribution and $\Theta[x]$ is the Heaviside step function. The slope, $\gamma = 2$, employed in this model corresponds with hard icy surfaces in the case of Europa while an intermediate value, $\gamma = 1.7$, is assumed for Ganymede (Krivov et al., 2003; Koschny and Grün, 2001a). To represent an icy regolith surface, we would set the initial ejecta speed distribution slope to a shallower value (e.g. $\gamma = 1.2$). The slope mainly affects the number of ejecta that can reach a given altitude while having a small effect on the distribution of ejecta launch sites on the surface. The difference between a hard icy surface and icy regolith would not substantially affect the conclusions of this study, which relies on the fraction of detections from a feature rather than absolute numbers. We assume no dependence between the initial speed at the surface and size of the ejecta particles (Sachse et al., 2015).

The ratio of kinetic energy carried by the ejecta to that of the impactors, K_e/K_i, must be less than unity. Since a portion of K_i is partitioned to comminution and heating, we assume $K_e/K_i \approx 0.3$ for Europa and Ganymede (Krüger et al., 2000). Taking into account the ejecta mass yield, Y, and the ejecta speed distribution slope, γ, energy conservation fixes u_0 via

$$K_e\bigg/ K_i = Y\frac{\gamma}{2-\gamma}\left(\frac{u_0}{v_{imp}}\right)^2\left\{\left(\frac{u_0}{u_{max}}\right)^{\gamma-2} - 1\right\}, \tag{8}$$

for $\gamma \neq 2$ and

$$K_e\bigg/ K_i = 2Y\left\{\frac{u_0}{v_{imp}}\ln\left(\frac{u_{max}}{u_0}\right)\right\}, \tag{9}$$

for $\gamma = 2$. A limited range of speed is necessary, otherwise energy carried by the ejecta would be infinite. To close the energy integral, we adopt $u_{max} = 3$ km/s, which is larger than the escape speed from either moon (Krüger et al., 2000).

We assume that the initial ejecta velocities are uniformly distributed in a cone with an opening half angle, ψ_0, relative to the surface normal

$$f_\psi = \frac{\sin\psi}{1-\cos\psi_0}\Theta[\psi_0 - \psi] \tag{10}$$

(Krivov et al., 2003).

The azimuthal angle, λ, about the normal (i.e. radial) vector is uniformly distributed ($\lambda \sim U[0, 2\pi]$). The relation between the velocity distribution of ejecta particles at the launch site on the surface and their velocities at a point **r** near the moon above the surface is illustrated in Fig. 1. The parameters for the ejecta model used in our simulations are summarized in Table 1.

2.2.1. Phase space distribution

Two versions of the ejecta cloud model, the spherically symmetric and asymmetric case, have been investigated by Krivov et al. (2003) and Sremčević et al. (2003), respectively. We focus on the spherically symmetric case since this is generalizable in terms of backtracking the ejecta trajectories to the surface. Asymmetries in the impactor flux at the moon lead to a modulation of ejecta number density as a function of colatitude. The most important aspect of the ejecta cloud model, as shown in Section 3, for geological mapping is the phase space distribution of individual particle dynamics used for trajectory backtracking. While the asymmetric model affects the absolute number of detected ejecta particles for a given flyby location relative to the moon, the asymmetry does not significantly affect the dynamical phase space distribution of individual particles. This framework for modeling ejecta particle clouds is consistent with in situ dust detections by Galileo (Krüger et al., 2003).

Mutual interactions between ejecta particles can be safely rejected. Additionally, only the moon's gravitational influence is considered within the Hill radius
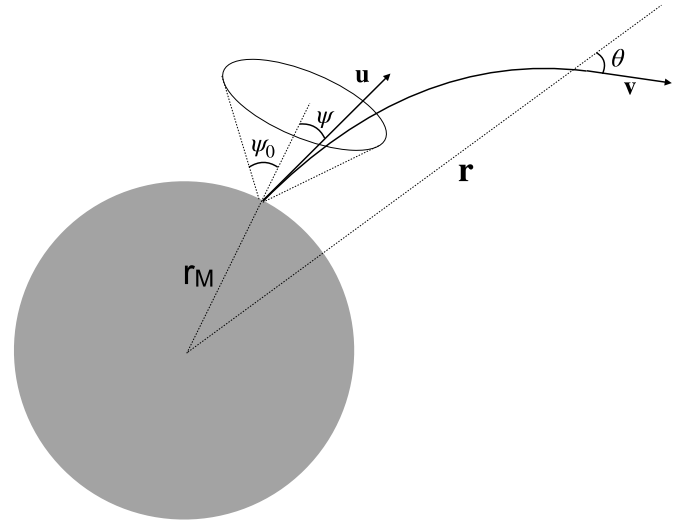

Fig. 1. Trajectory of a single ejecta particle from the launch site at the surface to a point **r** near the moon. An impact at the surface launches the individual ejecta particles at an angle ψ, distributed within the cone with opening half-angle ψ_0, and speed $|\mathbf{u}|$. The distribution for ψ and u at the surface are mapped to a distribution for θ and **v** at a detection point **r** via the Jacobian as in Eq. (12).

$$r_{Hill} = a\left(\frac{M_m}{3M_J}\right)^{1/3}, \tag{11}$$

where M_m is the mass of the moon and a is its mean orbital distance from Jupiter. The ejecta model ignores any dissipative forces. Since the ejecta dynamics is governed by the two-body problem, the phase space volume is conserved (Deriglazov, 2017). This enables the mapping of the distribution of ejecta velocities (Fig. 1) at the surface, $n(u, \psi)$, to the distribution at location r, $n(r, v, \theta)$, by

$$n(r, v, \theta) = n(u, \psi)\left|\frac{\partial(u, \psi)}{\partial(v, \theta)}\right| \tag{12}$$

The phase space density function is derived for the bound and unbound population separately to give the total number density of the ejecta cloud as a function of radial distance:

$$n(r) = n_{bound}(r) + n_{unbound}(r). \tag{13}$$

Bound particles are on elliptical trajectories while unbound particles are launched above escape speed and are on hyperbolic trajectories with respect to the moon. Fig. 2 shows the ejecta cloud number densities plotted as a function of altitude for Europa and Ganymede.

3. Flyby simulation method

In our simulations, the flybys are based on the trajectory of a spacecraft on a Jovian orbit while performing close encounters with the Galilean satellites (Lam et al., 2018). In the body fixed frame of the moon, the spacecraft trajectory can be approximated as a straight line with a pre-determined Closest Approach (C/A) altitude. The flyby speeds are on the order of several km/s while ejecta particle speeds are typically less than a few hundred m/s relative to the moon. Additionally, the particles are most likely encountered at the turnaround point along their trajectory due to their longer residence time. Therefore, the encounter speed is dominated by the spacecraft speed while the direction of the oncoming flux of ejecta in the spacecraft frame is from the apex direction (i.e. antiparallel to the spacecraft velocity vector with respect to the moon). The apparent direction from which the ejecta particles arrive at the instrument is referred to as the "dust ram" direction.

Here, we assume the dust analyzer looks in the spacecraft apex direction, which is the same as the dust ram direction in the body-fixed

Table 1
Ejecta model parameter values used in this study.

Satellite	G_{sil}	K_e/K_i (%)	u_0 (m/s)	γ	α	M^+ (kg/s)	Y	R_m (km)	v_{esc} (km/s)
Europa	0	30	29	2	12/5	554	1.7×10^4	1560.8	2.025
Ganymede	30	30	40	1.7	12/5	248	3.9×10^3	2631.2	2.741
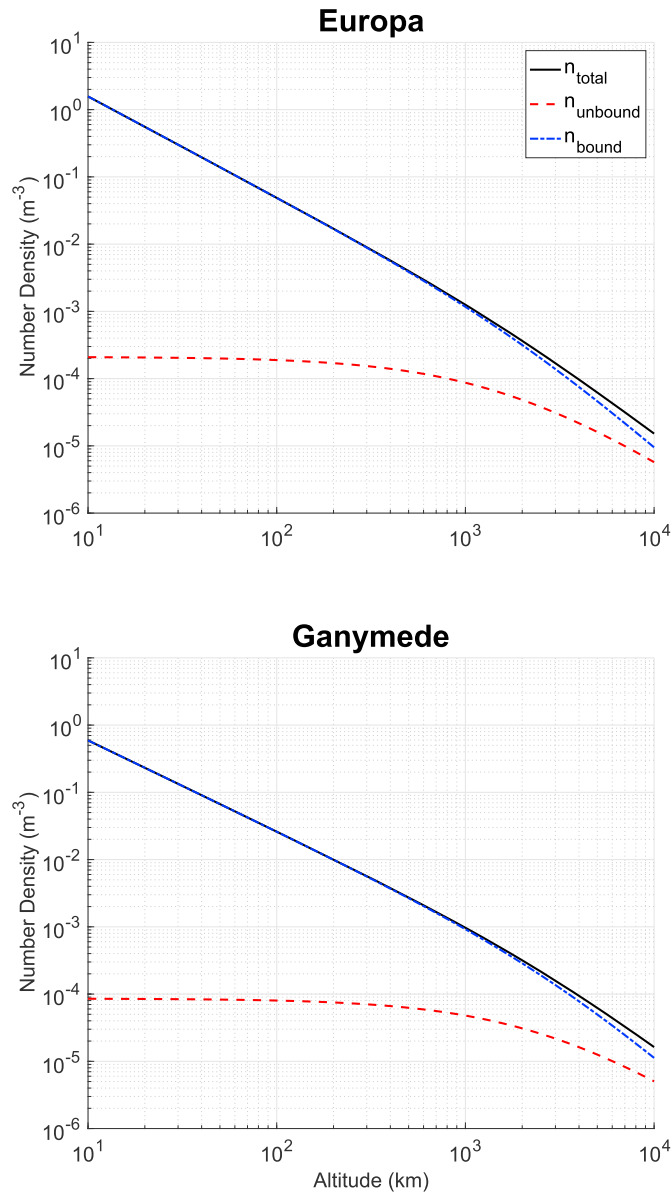
Fig. 2. Model number density of the ejecta cloud around Europa and Ganymede for particles > 200 nm. The densities for bound and unbound particles are calculated using Eqs. (42) and (53) by Krivov et al. (2003). The curves for both moons employ an opening cone half-angle, $\psi_0 = 30°$ along with the parameters in Table 1. Due to the higher silicate content in Ganymede's surface ice and subsequently lower ejecta mass yield, the number density is noticeably lower than Europa's.

in the apex direction (i.e. into the oncoming flux of ejecta particles) at C/A. Consequently, the sensitive area of the instrument varies as a function of time, attenuating the detection rate away from C/A. An ideal instrument would always perceive the total flux by pointing in the dust ram direction. The detection rate in both the time-varying and dust ram pointing scenarios falls off away from C/A primarily due to the decreased number density of the ejecta cloud at higher altitudes. Therefore, the difference between time-varying and dust ram pointing is not very large (Fig. 3). For simplicity, we consider only the dust ram pointing case where the sensitive area remains constant.

Using the flyby geometry shown in Fig. 3, the position and radial distance of the spacecraft is a function of time throughout the flyby given
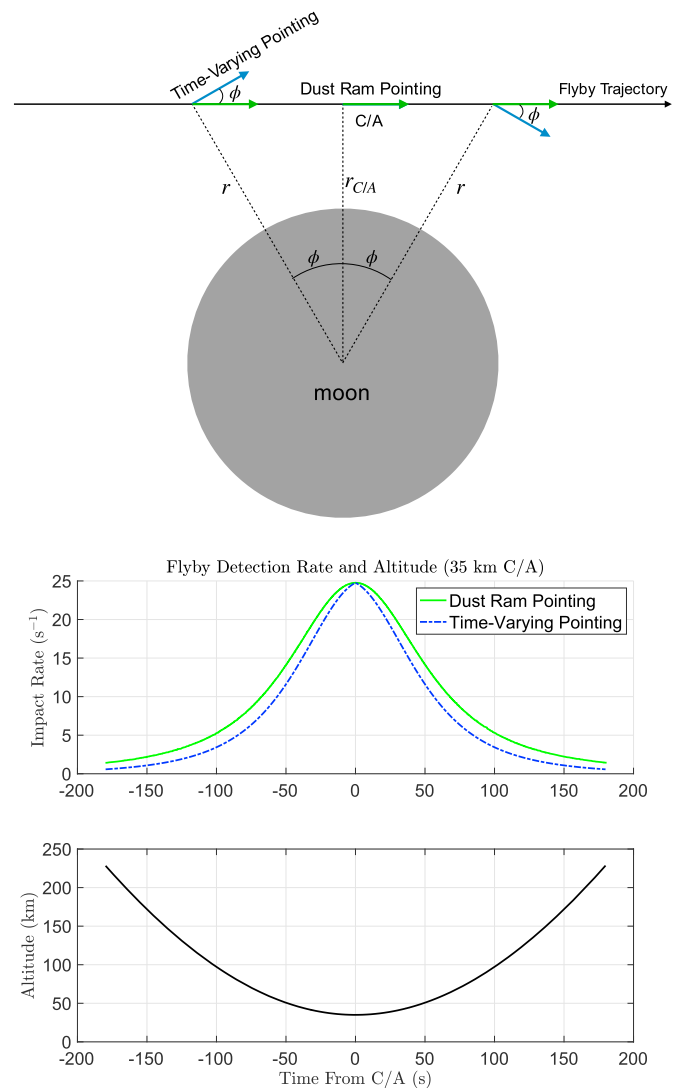

Fig. 3. "Ideal" flyby trajectory (top) showing both time-varying pointing, to accommodate nadir pointing for other instruments, and dust ram pointing (not to scale). The detection rate along with time and altitude is shown for an example flyby over Europa ($\psi_0 = 30°$) with a Closest Approach (C/A) altitude of 35 km. A 6 min interval centered on C/A is used here. This is based on SUDA aboard Europa Clipper: $v_{sc} = 4.5$ km/s with respect to the moon, $A_{sens} = 225$ cm^2, and detection threshold of 200 nm.

frame of a moon that is on a circular orbit (For Europa Clipper, the maximum difference between apex and ram direction is on the order of 2°). Due to the complexity of multi-instrument missions, this is often not feasible. Another possibility is nadir tracking where the dust analyzer boresight points 90° from nadir with a time-varying angle, φ, from the apex direction. The spacecraft slews to maintain nadir pointing for the remote sensing instruments such that the dust analyzer boresight points

by

$$r(t) = [0, v_{sc} \cdot t, r_{C/A}] \tag{14}$$

and

$$r(t) = \sqrt{(v_{sc} \cdot t)^2 + r_{C/A}^2}, \tag{15}$$

where $r_{C/A}$ is the radial distance of the spacecraft at C/A and t is the time from C/A. In this case, the spacecraft position and instrument boresight pointing are constrained to the xz-plane of the moon's body fixed frame. While a flyby over a particular feature will of course not necessarily fall within the xz-plane, this trajectory can be generalized to an arbitrary

flyby of the same type (i.e. straight line in the body-fixed frame of the moon). We therefore utilize this geometry in our simulations.

4. Simulated ejecta particle detections

Detections of ejecta particles by the dust analyzer in the vicinity of the moon occur stochastically and are described by a Poisson distribution, where the time between successive detections, Δt, follows an exponential distribution,

$$p(\Delta t) = \mu e^{-\mu \Delta t}. \tag{16}$$

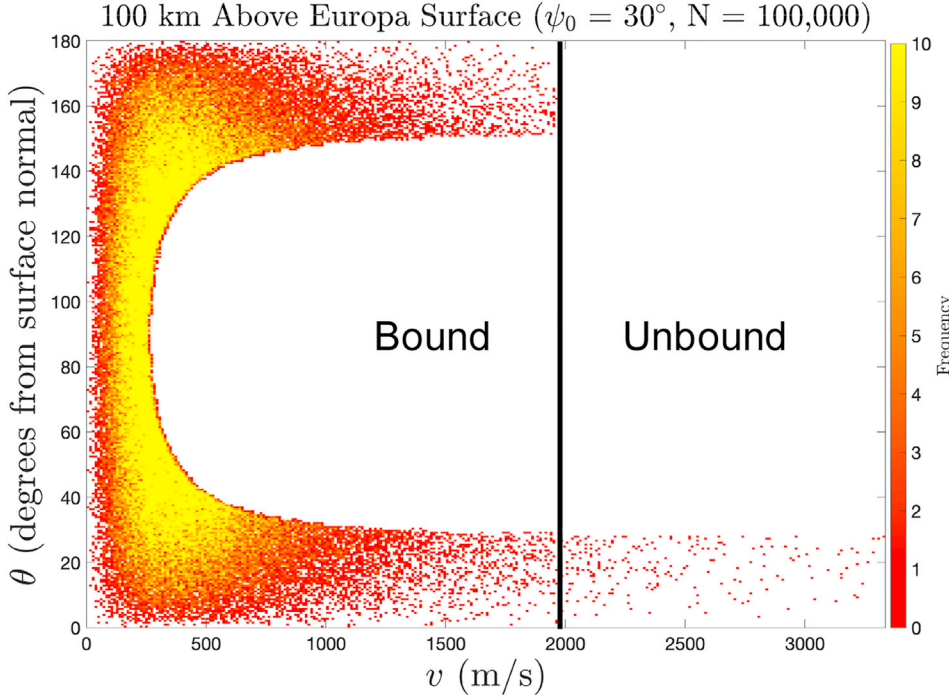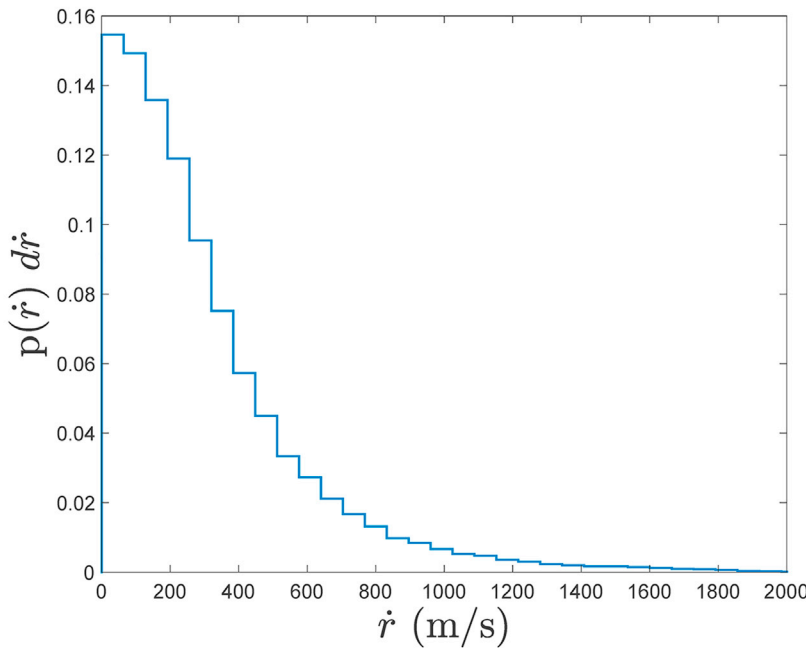Here, the average impact rate, μ, is a function of the ejecta cloud number

Fig. 4. (Upper panel) A bivariate histogram of random velocity components, v and θ, of ejecta 100 km above Europa. The azimuthal component, λ, is uniformly distributed and is not shown. Note the relatively rare occurrence of escaping particles in the lower right where $\theta < 90°$ since escaping particles never have returning trajectories. The seam of red points on the inside of the bound region is a plotting artifact. (Lower panel) The corresponding distribution for the radial component of the ejecta speed, $\dot{r}$, with respect to the moon. The most likely radial speed is zero since the ejecta cloud is dominated by bound particles near the turnaround point along their trajectories.

density, effective instrument sensitive area, and spacecraft speed: $\mu = A_{sens} \cdot v_{sc} \cdot n(r(t))$. Since the ejecta cloud density is a function of radial distance from the moon, the average impact rate is then a function of time leading to a time dependence of the exponential distribution itself. However, the rate at which this change occurs is small near C/A, where the detection rate peaks. Indeed, changes in the spacecraft's radial distance between detections (occurring at a rate of tens per second) are typically small (<1 m) during the time interval when 90% of detections occur. During this period, $\mu(t_0 + t_1) - \mu(t_0) \approx 0$, and thus $\mu(t)$ is approximately constant from one detection to the next. This is shown by the similarity between the number of stochastically simulated detections, N_{stoch}, and the deterministic number of detections given by

$$N_{det} = A_{sens} v_{sc} \int_{t_0}^{t_f} n(r(t)) dt, \tag{17}$$

where $N_{stoch} \approx N_{det} \pm \sqrt{N_{stoch}}$ and $[t_0, t_f]$ is the time interval over which the dust analyzer is sensitive to detections.

Incorporating a typical instrument field-of-view and shielding grids, where certain ejecta particles are missed due to high entry angles, does not have a significant effect on the results of this study. We therefore model the general case of a hemispherical half-flat-plate detector.

For each detection in the time series, a random velocity of the ejecta particle is drawn from the speed probability density

$$p(v, \theta | r) \propto \frac{\gamma \tilde{u}_0^\gamma}{1 - \cos \psi_0} \frac{\tilde{u}(\tilde{v})^{-\gamma - 4}}{\cos \psi(\tilde{v}, \theta)} \times \Theta[\psi_0 - \psi(\tilde{v}, \theta)] \Theta\left[\tilde{u}(\tilde{v}) - \tilde{u}_0\right] \tilde{v}^2 \sin \theta \tag{18}$$

at a radial distance, r, which follows directly from the phase space number density (Eq. (12)). The variables $\tilde{v} = v/v_{esc}$, $\tilde{u} = u/u_{esc}$, and $\tilde{u}_0 = u_0/v_{esc}$, are used where v_{esc} is the escape speed at the surface. Here, v is the speed of the particle and θ is the angle between the particle's velocity vector and the radial position vector at the point of detection. Fig. 4 shows an example bivariate histogram of 100,000 randomly drawn (v, θ) pairs from the joint probability density (Eq. (18)) at an altitude of 100 km above Europa's surface. The azimuthal angle, λ, about the radial vector is drawn from a uniform distribution, $(\lambda \sim U[0, 2\pi])$. These three random variables form the velocity vector, $[v, \theta, \lambda]$, defined at the position of detection in spherical coordinates corresponding to the vector, $[v_x, v_y, v_z]$, in the moon's body fixed frame in Cartesian coordinates.

The simulated detections all take place well within the Hill sphere of the moon. The speed of a typical particle is much lower than the escape speed (Fig. 4), which results in their turning points being lower than the Hill radius of the moon. Therefore, third body gravity forces are ignored. Additionally, the typical ejecta lifetime of < 1 h is much shorter than the rotation period of Europa or Ganymede (3.55 days and 7.15 days respectively). Therefore, we treat the moons's body fixed frame as an inertial frame for ejecta particle two-body dynamics.

The time series from the exponentially distributed time steps for the corresponding spacecraft positions at each detection is associated with the random ejecta velocities at each position to form randomly generated $[r, v]$ state vectors in the moon's inertial frame for each simulated ejecta particle. From this, the orbital elements for each ejecta particle are calculated to determine the Keplerian trajectory back to the surface launch site. Using the methods described in the next section, we generate random ejecta launch sites for each detection throughout a simulated flyby.

5. Mapping ejecta particle detections to surface features

Dust analyzers, such as SUDA, register a time series of chemical spectra from the ejecta particles detected during the flyby while the exact sites of origin are otherwise unknown. The velocity distribution (Eq. (18)) from the ejecta cloud model constrains the possible surface launch sites to an area near the spacecraft's groundtrack. We utilize simulated launch sites based on backtracked random velocities to derive the expected time series of detections originating from a single geological feature.

Europa Clipper will perform low altitude flybys over geological features of interest. While over the feature, SUDA will collect material ejected from both inside and outside the feature. As an example, Fig. 5 shows the groundtrack of a flyby over Thera Macula, which is a roughly 100 km diameter feature in Europa's southern hemisphere with a morphology that suggests recent vertical deformation and collapse leading to the extrusion of subsurface material (Mével and Mercier, 2007).

The simulated flyby is based on the 6th Europa flyby in the Clipper reference tour (19F23v2). The C/A altitude is 35 km over the feature as shown in the top two plots. For a single MC run, the random sequence of ejecta particles detected by SUDA are backtracked to their launch sites on the surface (Fig. 5 left panels). The random variates for the MC simulation are the detection times and ejecta particle velocities based on the model (Krivov et al., 2003).

We assume the composition of particles originating from the feature are distinct from that of the surrounding area. We denote detections from the feature as having composition "Type A" while the surrounding composition is "Type B". The plots in the right panels of Fig. 5 show the sequence of detections for this particular MC run.

To demonstrate the flyby altitude dependence, we raised the C/A altitude to 100 km and perform another MC run of SUDA detections shown in the bottom two plots. Not only does the total number of ejecta detections decrease due to the lower particle density at higher altitudes, but the sequence of Type A detections gets washed out by those from the surrounding area, due to larger mixing of particle sites of origin at higher altitudes. This makes it more difficult to associate Type A detections in the SUDA data set with a surface feature. Clearly, SUDA's ability to resolve the composition of geological features is a function of both the flyby altitude and the size of the feature itself.

To facilitate deriving the composition of a feature, we examine typical cases of flyby trajectory altitudes over a feature of a given size to guide flyby design. This is done by performing MC simulations of Clipper flybys over hypothetical circular surface features. The C/A sub-spacecraft point is located at the center of the feature for each flyby scenario. The MC flyby simulations are performed under two varying parameters: C/A altitude and feature diameter, and repeated for 50 MC trials.

6. Quantifying feature detectability

The number of Type A (from inside the feature) detections relative to the total number of detections during the observation window over the feature (Fig. 6) is computed for various feature sizes and C/A altitudes ranging from 25 to 100 km with a 5 km step size. This fraction, referred to as the "detectability" of the feature, is expressed as

$$D = \frac{\langle N_A \rangle}{\langle N_{total} \rangle}, \tag{19}$$

where $\langle N_A \rangle$ is the expected number of Type A detections and $\langle N_{total} \rangle = \langle N_A \rangle + \langle N_B \rangle$, the expected number of all detections acquired over the feature.
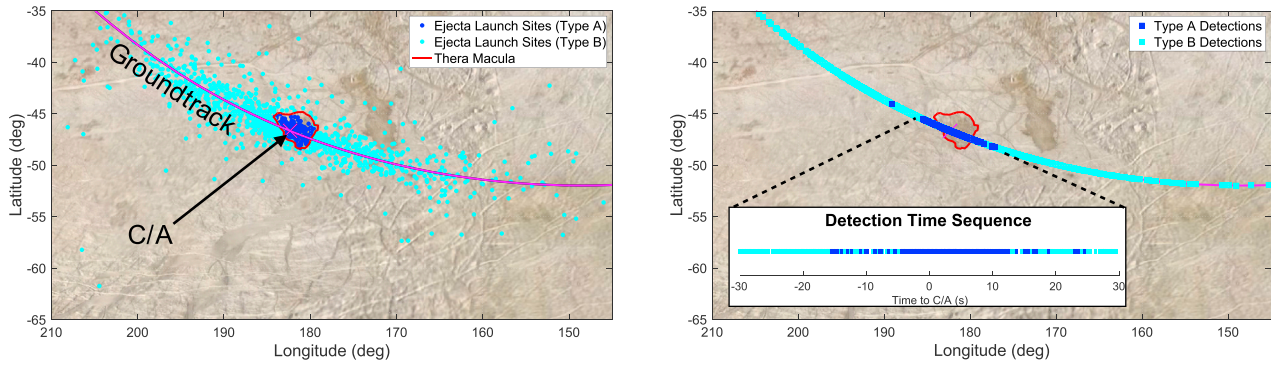
$\langle N_A \rangle$ and $\langle N_{total} \rangle$ are the mean values from 50 MC trials of flyby detections over circular features for each C/A altitude. The uncertainty for both, $\langle N_A \rangle$ and $\langle N_B \rangle$, is computed as the error of the mean with a 0.95 confidence

$$\delta N_A = 1.65 \frac{\sigma_A}{\sqrt{n}}, \tag{20}$$

and

$$\delta N_B = 1.65 \frac{\sigma_B}{\sqrt{n}}, \tag{21}$$

35 km Flyby over Thera Macula

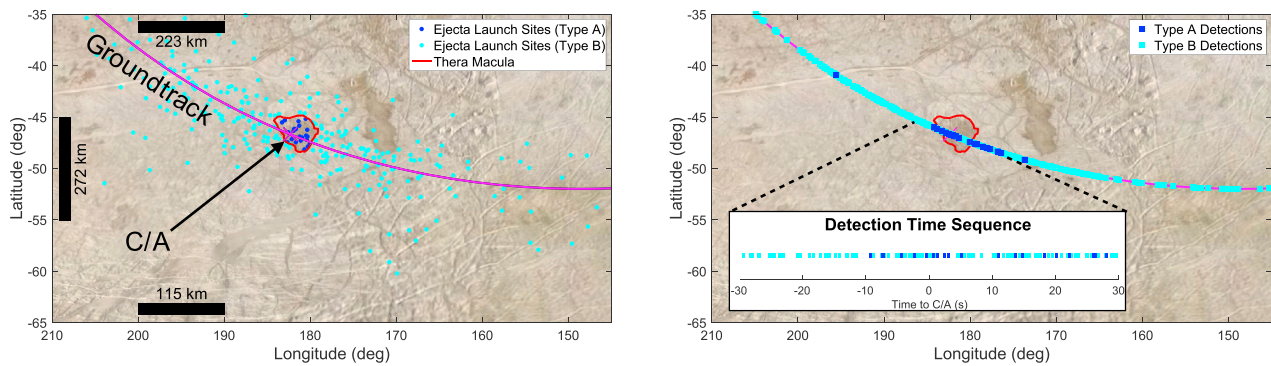

100 km Flyby over Thera Macula

Fig. 5. A single Monte Carlo (MC) run for SUDA detections during a flyby over Thera Macula. This particular flyby trajectory is the sixth Europa flyby in the 19F23v2 tour design. The left plot shows the locations of origin on the surface of the grains detected by SUDA. The right plot shows where the same particles are detected by SUDA. The detections marked in dark blue color originated from inside Thera Macula and those in light blue color originated from outside the feature. The C/A sub-s/c point is close to the center of the surface feature making this an ideal trajectory for mapping the composition of Thera Macula. The top two plots are for the baseline 35 km flyby. The bottom two plots show a separate MC run with a modified C/A altitude raised to 100 km.
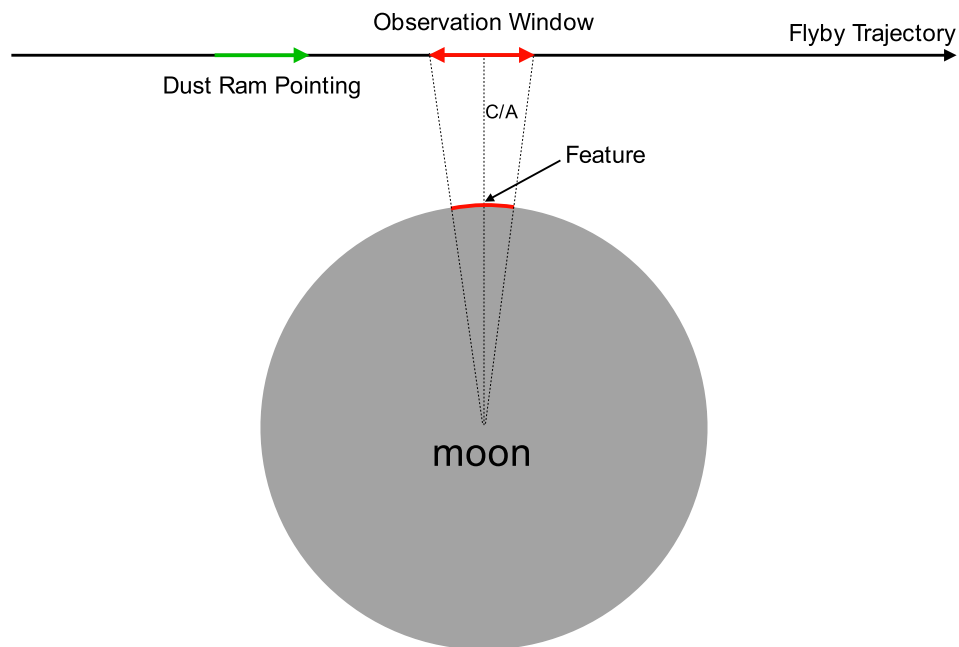

Fig. 6. The observation window is defined as the segment of the flyby where the spacecraft is over the feature. It is during this time that we expect the best chance of detecting ejecta particles originating from the feature.

where σ_A, σ_B are the sample standard deviation of N_A and N_B respectively and n is the number of MC trials (Thomopoulos, 2013). Since $\langle N_{total} \rangle$ is dependent on $\langle N_A \rangle$ and $\langle N_B \rangle$, the uncertainty is simply

$$\delta N_{total} = \delta N_A + \delta N_B. \tag{22}$$

We find that the detectability, derived from Eq. (19), for Europa and Ganymede (Figs. 7 and 8) follows a power law, where the slope depends on feature size. The detectability model is therefore formulated as a function of both the C/A altitude, a, and the surface area of the feature, s,

$$D(a,s) = \left(\frac{a + R_M}{R_M} \right)^{k\tilde{s}^\beta}. \tag{23}$$

where k and β are constants, $\tilde{s} = s/2\pi R_M^2$, and the surface area of the feature is given by
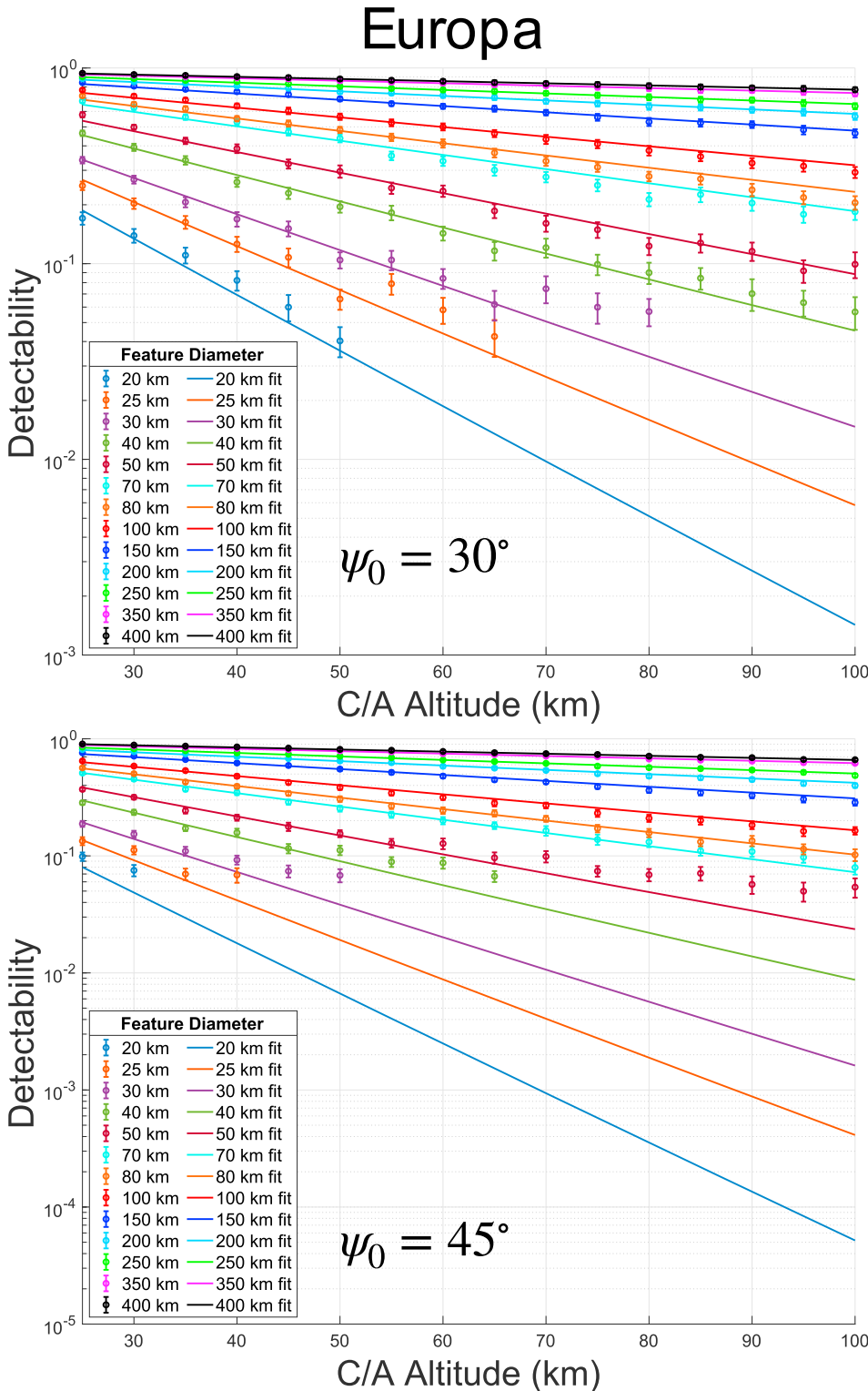

Fig. 7. Detectability for Europa flybys. The data from each series of MC trials for a given C/A altitude and feature diameter (increasing from bottom to top) are fit to a single power law (Eq. (23)). For $\psi_0 = 30°$ (top), the ejecta are launched closer to the normal direction with respect to the surface. This results in more detections closer to the sub-spacecraft point. A dust analyzer can expect better resolution of feature composition time series in the case where $\psi_0 = 30°$, especially for small features (<70 km in diameter). Wider launch angles lead to larger mixing in the ejecta cloud, which decreases detectability since particles are more likely to originate farther away from the sub-spacecraft point on the surface. The data no longer follow a power law for small features in the $\psi_0 = 45°$ case.
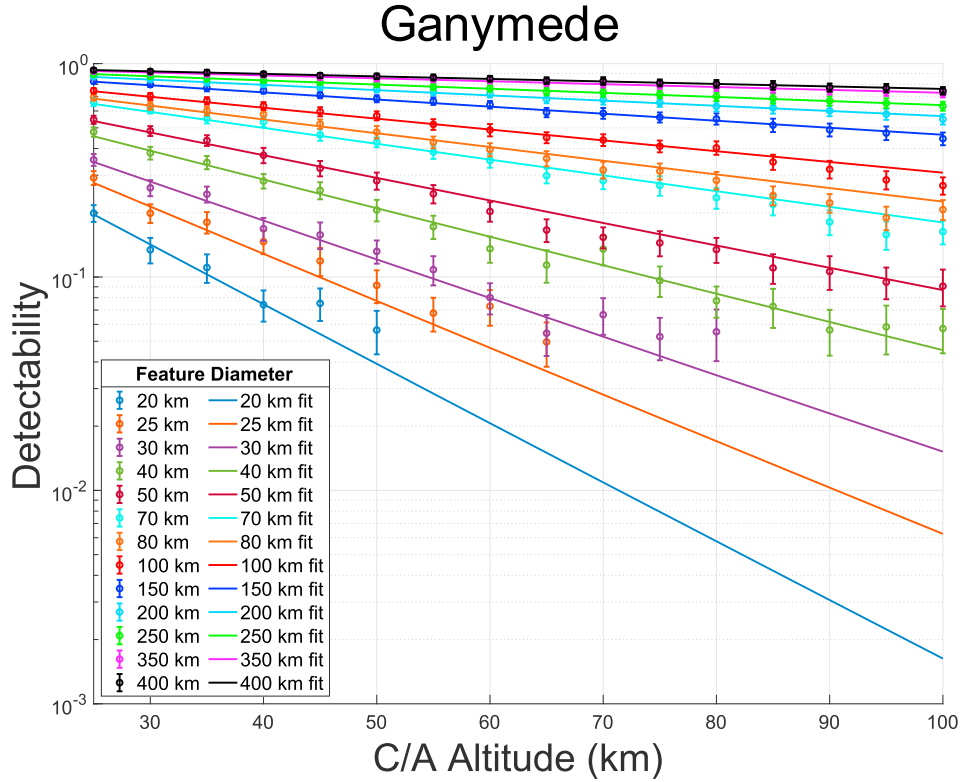
Fig. 8. Detectability data for Ganymede are very similar to that of Europa for $\psi_0 = 30°$. The data follow the power law for feature diameters $>= 50$ km. Data for smaller features (bottom) tend to deviate from the power law slope above certain altitudes. The reason for this is explored in section 6.1.1.

$$s = 2\pi R_M^2 (1 - \cos(d / 2R_M)). \tag{24}$$

The model is arranged such that the slope depends on the feature surface area scaled by the surface area of the moon's hemisphere, where d is the diameter of the circular feature.

The parameters of this power law (Table 2) are derived from flyby simulations using the ejecta cloud model parameters shown in Table 1.

To show the effect of the ejecta plume opening cone half-angle, ψ_0, on detectability, we examine the case of $\psi_0 = 30°$ and $45°$ for Europa. $\psi_0 = 45°$ corresponds to larger mixing of the ejecta cloud particles as well as degraded spatial resolution for mapping the composition of surface features. It is reasonable to assume that ψ_0 is closer to $30°$ for both moons based on data returned by the Galileo spacecraft (Sremčević et al., 2005) as well as laboratory experiments of hypervelocity impacts on ice-silicate mixtures by Koschny and Grün (2001a). For Ganymede, we present the case where $\psi_0 = 30°$.

6.1. Discussion

6.1.1. Characteristics of the data and model

We plotted the data (Figs. 7 and 8) to cover a wide range of feature sizes (20–400 km) and C/A altitudes (25–100 km). For small features at high altitudes, the data no longer follow a power law. Data for small features (<50 km) are excluded from the model fit beyond an altitude where the detectability trend deviates sharply from the power law. Fig. 10 shows the data for the entire C/A altitude range (25–100 km) over a feature with a 20 km diameter. To identify the reason for the distinct

Table 2
Feature detectability parameters.

Satellite		k	β
Europa	$\psi_0 = 30°$	-0.304 ± 0.003	-0.542 ± 0.001
	$\psi_0 = 45°$	-0.53 ± 0.01	-0.530 ± 0.003
Ganymede	$\psi_0 = 30°$	-0.336 ± 0.007	-0.527 ± 0.003

deviation at a certain altitude, we examine the geometry of the modeled ejecta velocities at the launch points.

Fig. 9 shows the geometry of the ejecta launch angles given by the distribution in Eq. (10). For ejecta launched on the average angle, $\langle \psi \rangle$, from the surface normal, particles originating from a relatively small feature will not be detected within the observation window over the feature. Only ejecta particles launched at small angles, which are relatively rare, are detectable at or above the "breakdown" altitude. This phenomenon appears in the simulation data corresponding to small features (Fig. 10 upper panel). Using the geometry shown in Fig. 9, we can approximate the point at which the data depart from the power law behavior as

$$a_b \approx \frac{f_d}{\tan \langle \psi \rangle}, \tag{25}$$

where a_b is the breakdown altitude and f_d is the feature diameter. Data corresponding to an altitude $>= a_b$ are excluded from the fit (Eq. (23)).

For comparison, the relative number of ejecta particles detected at C/A that are Type A (i.e. C/A detection fraction) is also shown for each altitude in Fig. 10. These values are found using the distribution of ejecta launch site distances from the sub-spacecraft point on the surface of the moon (Fig. 11), derived using MC simulations of ejecta trajectories at each detection altitude. The C/A detection fraction is approximately the same as the detectability from the flyby for small features ($\sim < 50$ km diameter) at all C/A altitudes (Fig. 10 upper panel). Recall, the detectability is the relative number of Type A detections collected throughout the observation window over the feature. For larger feature sizes (e.g. 80 km), the C/A detection fraction is higher than flyby detectability at low altitudes (Fig. 10 lower panel). As the C/A altitude increases over an 80 km feature, the C/A detection fraction and the detection fraction from the flyby observation window begin to merge. The reason for this is best seen in the time series of detections for both the 20 km and 80 km feature size examples on Europa (Fig. 12).
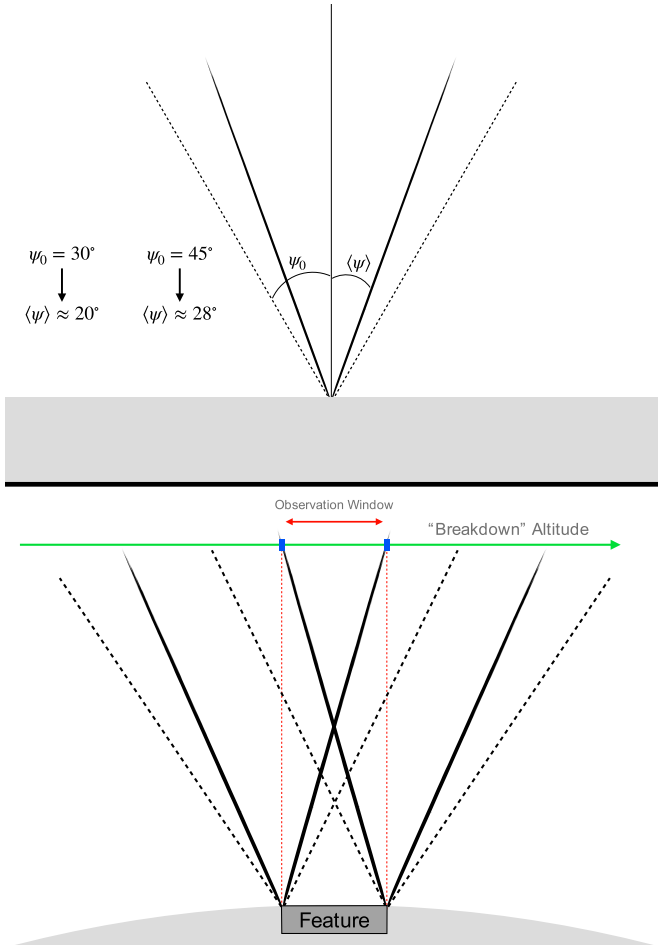
Fig. 9. (Top) Geometry of ejecta launch angles. The ejecta cone opening half-angle, ψ_0, is shown with its corresponding average launch angle, $\langle\psi\rangle$. (Bottom) Ejecta particles launched at the average angle (solid lines) are not detected above the "breakdown" altitude of the trajectory for small features. This is a limiting case in the model where the feature is too small for ejecta particles to reach detection points over the feature on average launch angle trajectories.

For the 20 km feature (Fig. 12 (a) and (b)), the time series of Type A detections (i.e. particles originating from the feature) is relatively flat and uniform throughout the observation window for both low and high C/A altitudes. The prevalence of Type A detections is therefore roughly the same near the edges of the observation window as at C/A throughout the altitude range: [25 km, 100 km].

For the 80 km feature (Fig. 12 (c) and (d)), low C/A altitudes have a distinct peak in Type A detections centered at C/A during the observation window (Fig. 12 (c)). The low Type A detection near the edges of the observation window attenuates the flyby detectability. At higher C/A altitudes (Fig. 12 (d)), the Type A detection flattens out approaching the same characteristic as that of the smaller feature sizes, causing the integrated detection to approach that of the C/A detection as can be seen for higher altitudes in Fig. 10 (lower panel).

Both the change in slope for detections from small features at a breakdown altitude and the relation between the C/A detection fraction and the detectability over the observation window are demonstrated to be consequences of the ejecta cloud model and the flyby geometry. The validity of our detectability model is restricted to the domain of C/A altitudes and feature diameters used to derive its parameters.

6.1.2. Implications for compositional mapping

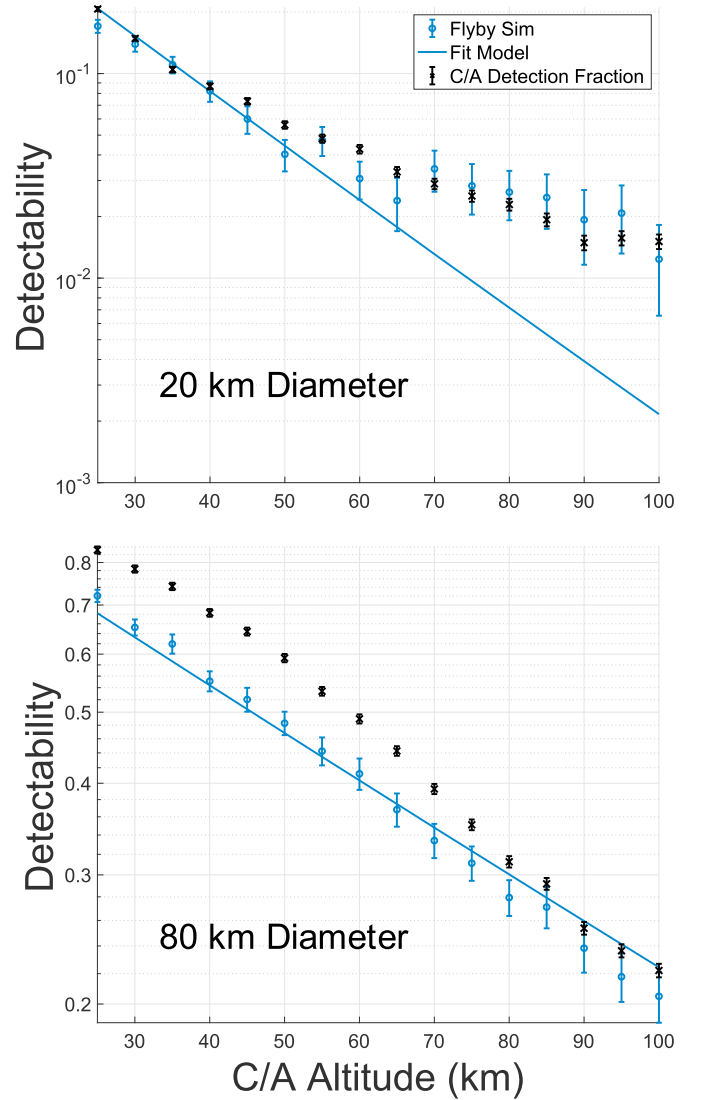Our model, derived from our simulation, is a useful tool for assessing

Fig. 10. Limiting case in the model where the feature is too small for ejecta particles to reach detection points over the feature on average launch angle trajectories illustrated in Fig. 9. The case shown here is for Europa where $\psi_0 = 30°$. The detectability of the 20 km diameter feature (upper panel) shows two distinct characteristics: (1) it tracks with the detectability at C/A and (2) there is a deviation from the power law (Eqn. (23)) at around 55 km C/A altitude. The first characteristic is due to the feature being so small that the integration of detections over the feature are similar to taking place only at C/A. The second characteristic is due to the ejecta launch angles at $\langle\psi\rangle$ from the feature's outermost edge being undetectable beyond a "breakdown" altitude (~ 55 km in this case). Data at or above the breakdown altitude are excluded from the fit. The 80 km diameter feature (lower panel) is large enough such that this breakdown in detectability slope does not occur in the C/A altitude domain explored here. The integrated detectability from the flyby simulations is below the C/A detectability for low altitudes until they both merge at higher altitudes.

how well a feature's composition can be resolved in a time series of chemical spectra acquired by a dust analyzer. Detectability, as defined in Section 6, is a quantitative description of the prevalence of spectral data that can be acquired from the surface of the feature. The MC trials performed here show the implications of the ejecta cloud model and its parameters.

Clearly, ψ_0 has a significant effect on detectability. The steeper slopes (corresponding to the case where $\psi_0 = 45°$) imply that resolving a surface feature requires lower C/A altitudes. This is expected since a wider distribution of ejecta launch angles from the surface produces broader
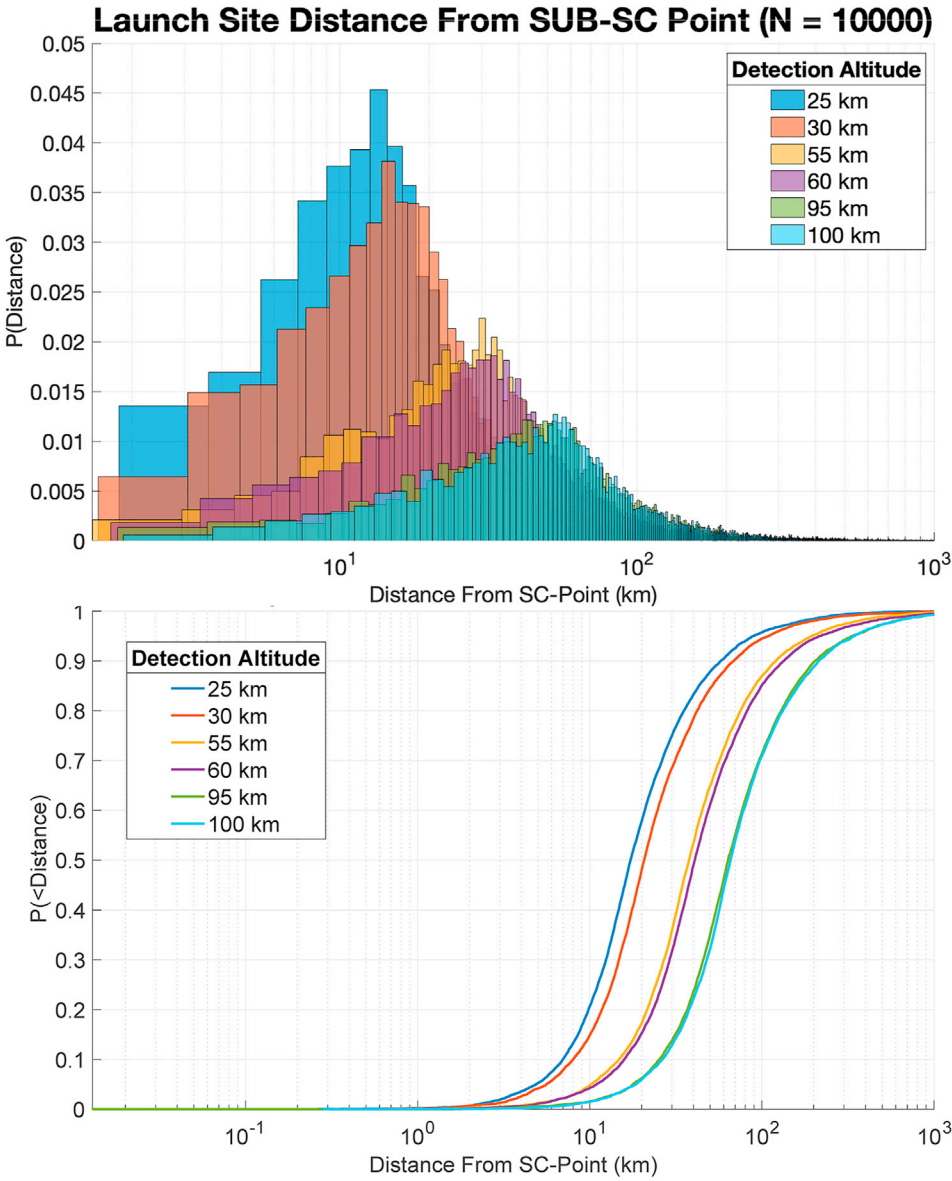
Fig. 11. The distribution of launch site distance from the sub-spacecraft (sub-sc) point on the surface is derived using random ejecta velocities at a given altitude from the pdf (Eq. (18)). Pairs of altitudes spaced by 5 km each are shown to represent low, mid, and high altitudes for the domain of this study. The distribution changes more significantly between altitudes in the lower range than for the higher range. The detectability of a feature at C/A as a function of altitude can be calculated from these distributions using the cumulative distribution function (bottom plot) where the distance from SC-Point is the radius of the feature. This gives the fraction of detections made at C/A that originate from the feature. The example distributions shown here are for Europa ($\psi_0 = 30°$).

mixing throughout the ejecta cloud, making it more likely to detect particles further away from the spacecraft groundtrack.

6.2. Application to flyby design

Our model (Eq. (23)) can be employed to constrain the maximum acceptable C/A altitude for a flyby directly over a feature:

$$a_{max}(D_{min}, \tilde{s}) = R_M \left(D_{min}^{\frac{1}{k}\tilde{s}^{-\beta}} - 1 \right), \tag{26}$$

where D_{min} is the minimum required detectability. If the required minimum detectability is, for example, 0.5 (i.e. the majority of detections originate from the feature) for a given feature size, the maximum acceptable C/A altitude, a_{max} can guide the flyby design in order to achieve the science goals driving D_{min}. Given the uncertainties in the parameters, δk and $\delta \beta$, the uncertainty for a_{max} is given by

$$\delta a_{max} = | \ln(D) D^{\frac{1}{k}\tilde{s}^{-\beta}} k^{-1} | \sqrt{\left(k^{-1}\tilde{s}^{-\beta}\delta k \right)^2 + (\ln(\tilde{s})\delta\beta)^2}. \tag{27}$$

The effect of uncertainties in the spacecraft's orbital trajectory on feature detection is examined in Appendix A.

As examples, Table 3 shows the maximum acceptable C/A altitudes for mapping the composition of features with select sizes on Europa and Ganymede.

7. Summary

In this paper, we have shown how to apply an ejecta cloud model to determine the requirements for deriving the composition of surface geology using a dust analyzer. In general, one can apply a known flyby geometry and instrument capabilities to predict the number of detections by a dust analyzer over a feature. To derive the expected detections that originate from the feature, MC simulations of the detections are applied, leading to a model that describes the ability of a dust analyzer to resolve the composition of a surface feature in the time series of spectral data obtained on an orbiting spacecraft.

The MC simulations utilize the velocity distribution of the ejecta particles allowing us backtrack their trajectories to the surface and compute the feature detection fraction as a random variate for each MC trial. The detection fraction quantitatively describes the ability to obtain chemical
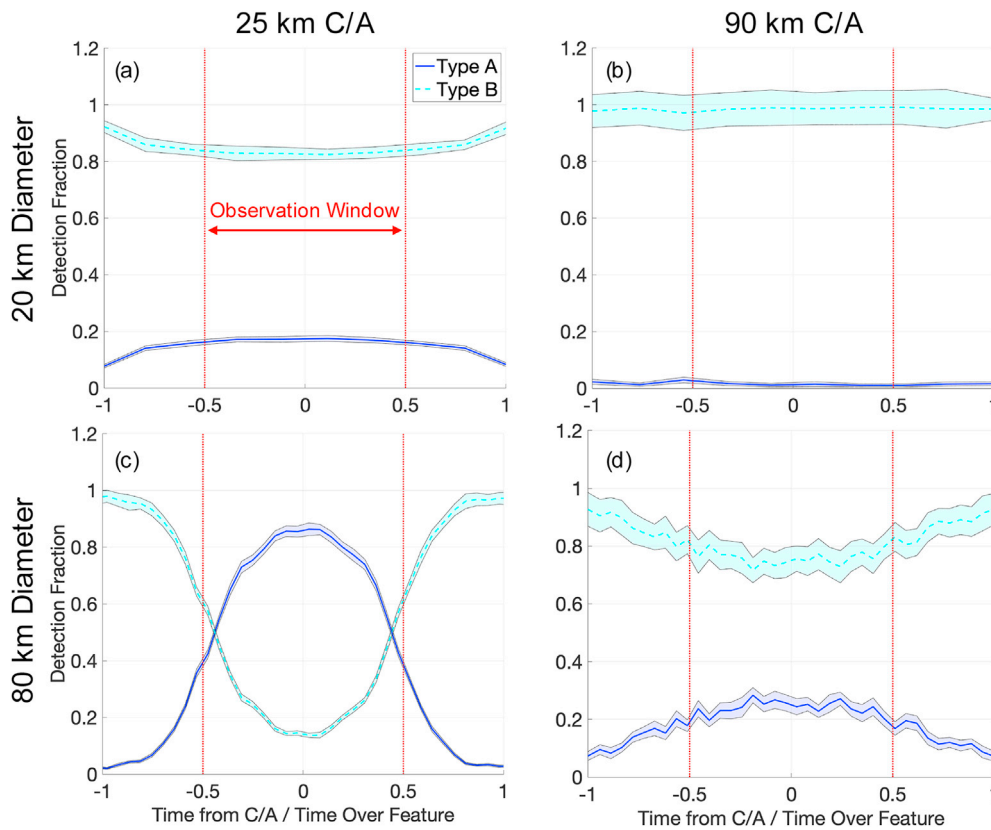
Fig. 12. The top two plots show the detection time series over a 20 km diameter feature at 25 and 90 km C/A altitudes while the bottom two plots show a flyby over an 80 km diameter feature. The value for $\langle N_A \rangle$ is based on the integration of the blue curve (Type A, originating from the feature) during the observation window. The shaded portion of the curves represents the $\sqrt{N_A}$ and $\sqrt{N_B}$ uncertainty from each time bin while the solid lines represent the average over 50 MC trials.

Table 3
Maximum acceptable C/A altitudes given $D_{min} = 0.5$

Satellite	Feature Diameter (km)	ψ_0	Max C/A Altitude (km)
Europa	50	30°	27.9 ± 0.03
		45°	18.04 ± 0.04
	100	30°	59.8 ± 0.02
		45°	37.79 ± 0.03
	200	30°	129.5 ± 0.02
		45°	79.66 ± 0.03
Ganymede	50	30°	27.99 ± 0.06
	100	30°	58.45 ± 0.05
	200	30°	122.8 ± 0.04

samples from a feature given its size and the C/A altitude. Since the detectability model provides the number of feature detections relative to the total number of detections over the feature during a flyby, it can be employed for either the time-varying or dust ram pointing scenario since the most significant difference between the two is the absolute number of detections based on the time-varying sensitive area of the instrument.

The detectability model is a useful tool for determining the flyby requirements over a geological feature of interest. It describes how one may access the composition of a surface feature via ejecta material sustained by micrometeoroid bombardment. Eq. (26) provides the maximum altitude to achieve the required detectability for meeting science goals. Mission planners can apply this model to design flyby trajectories on which a dust analyzer would be used to identify the composition of geological features.

Author statement

William Goode: Conceptualization, Methodology, Simulation and Data Analysis, Writing-Original draft preparation, Writing-Reviewing and Editing, Writing-Revising Manuscript.
Sascha Kempf: Conceptualization, Methodology, Writing-Reviewing and Editing, Writing-Revising Manuscript.
Juergen Schmidt: Writing-Reviewing and Editing, Writing-Revising Manuscript.

Declaration of competing interest

The authors declare that they have no known competing financial interests or personal relationships that could have appeared to influence the work reported in this paper.

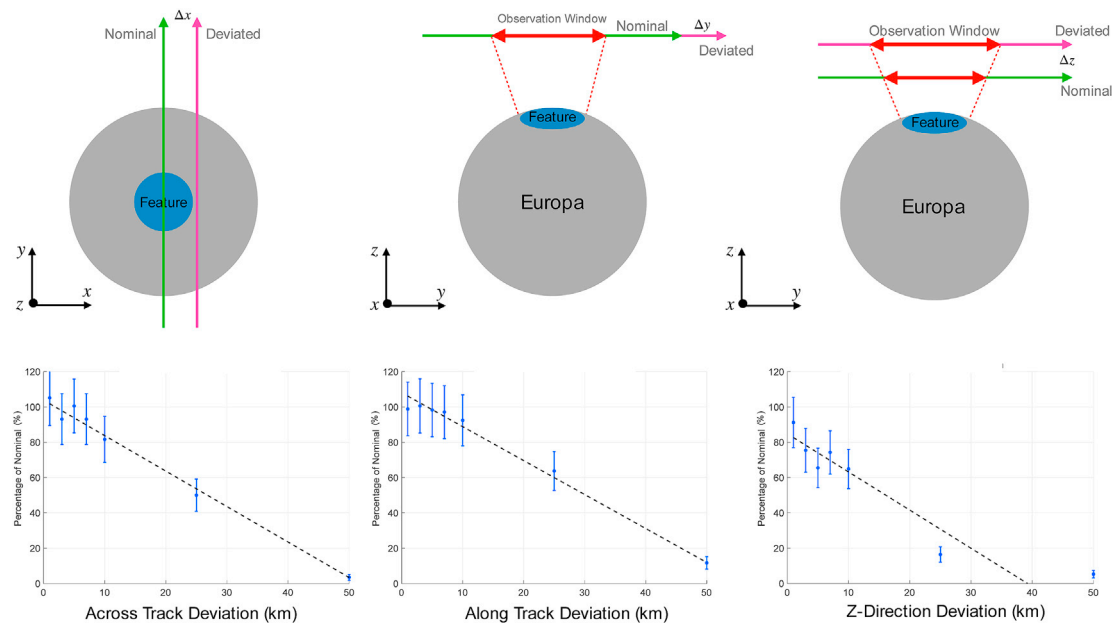**Appendix A. Orbital Uncertainty Effects on Feature Detection**

Fig. 13. Orbital uncertainty analysis is shown for deviations across track (left), along track (center), and in the z-direction (right). The black dashed lines indicate the linear fit to the data showing percentage of nominal as a function of deviation from nominal. The last two data points are excluded from the linear fit in the z-direction case since they do not plausibly fit a linear trend set by the first five data points.

The detectability model derived in this paper assumes a known spacecraft trajectory relative to the moon possessing the surface features we wish to compositionally characterize. Here we examine how uncertainties in the spacecraft's orbital trajectory may affect the detection of ejecta particles originating from a feature. Given the similarity between the models for both moons, we use a flyby over Europa to demonstrate the sensitivity of detection outcomes to orbital uncertainty.

We examine a case with a 25 km C/A over a 50 km diameter circular feature. This altitude and feature size are chosen since this case is sensitive to trajectory deviations, representing a typical flyby geometry for Europa Clipper. At higher altitudes, the launch site distributions are more spread out making trajectory deviations less consequential on detection origin. Larger feature sizes are intuitively easier to detect, therefore deviations also have less effect.

The effects of each deviation is quantified as a percentage of nominal. This analysis compares the number of feature particles collected by SUDA while over and/or adjacent to the feature (i.e. in the "observation window"). Deviations along the track shift the location of the observation window relative to nominal, which changes the number of feature particles that are counted in it thereby affecting our ability to map composition to the feature. If the spacecraft position is shifted forward or backward relative to the nominal trajectory, the instrument collects the same number of feature particles but is less effective in correlating them to the feature using the observation window. Deviations across the track results in fewer feature particle detections since the groundtrack itself covers less of the feature.

Fig. 13 shows that compositional mapping with a dust analyzer is robust against positional uncertainties of up to 5 km along and across the nominal trajectory. Assuming a flyby speed of 4.5 km/s relative to the moon, a 5 km positional uncertainty corresponds to a 1.1 s clock error. Uncertainties in the z-direction have a much larger effect as expected since the number density decreases with altitude while mixing of the ejecta cloud particles increases with altitude.

References

Carr, M.H., Belton, M.J.S., Chapman, C.R., Davies, M.E., Geissler, P., Greenberg, R., McEwen, A.S., Tufts, B.R., Greeley, R., Sullivan, R., Head, J.W., Pappalardo, R.T., Klaasen, K.P., Johnson, T.V., Kaufman, J., Senske, D., Moore, J., Neukum, G., Schubert, G., Burns, J.A., Thomas, P., Veverka, J., 1998. Evidence for a subsurface ocean on Europa. Nature 391 (6665), 363–365. https://doi.org/10.1038/34857.

Cassen, P., Peale, S.J., Reynolds, R.T., 1980. On the comparative evolution of Ganymede and Callisto. Icarus 41 (2), 232–239. https://doi.org/10.1016/0019-1035(80)90006-8, 0019–1035. https://www.sciencedirect.com/science/article/pii/0019103580900068.

Colombo, G., Lautman, D.A., Shapiro, I.I., Dec. 1966. The earth's dust belt: fact or fiction?, 2, gravitational focusing and Jacobi capture. J. Geophys. Res. 71, 5705–5717.

Deriglazov, A., 2017. Classical Mechanics, second ed. Springer International Publishing AG Switzerland.

Dikarev, V., Gruen, E., Baggaley, J., Galligan, D., Landgraf, M., Jehn, R., 2005a. The new ESA meteoroid model. Adv. Space Res. 35 (7), 1282–1289. https://doi.org/10.1016/j.asr.2005.05.014, 0273–1177, (Space Debris). https://www.sciencedirect.com/science/article/pii/S0273117705005983.

Dikarev, V., Gruen, E., Baggaley, J., Galligan, D., Landgraf, M., Jehn, R., 2005b. Modeling the sporadic meteoroid background cloud. Earth Moon Planets.

Dikarev, V., Gruen, E., Landgraf, M., Jehn, R., 2005c. Update of the ESA meteoroid model. In: Proceedings of the 4th European Conference on Space Debris. ESA, pp. 271–277.

Divine, N., 1993. Five populations of interplanetary meteoroids. J. Geophys. Res. 98, 17 029–117 048.

Goldsworthy, B.J., Burchell, M.J., Cole, M.J., Armes, S.P., Khan, M.A., Lascelles, S.F., Green, S.F., McDonnell, J.A.M., Srama, R., Bigger, S.W., 2003. Time of flight mass spectra of ions in plasmas produced by hypervelocity impacts of organic and mineralogical microparticles on a cosmic dust analyser. A&A 409 (3), 1151–1167. https://doi.org/10.1051/0004-6361:20031087.

Greeley, R., Klemaszewski, J., Wagner, R., 2000. Galileo views of the geology of Callisto. Planet. Space Sci. 48 (9), 829–853. https://doi.org/10.1016/S0032-0633(00)00050-7, 0032–0633. http://www.sciencedirect.com/science/article/pii/S003206330000050.

Grün, E., Staubach, P., 1996. Dynamic populations of dust in interplanetary space. Int. Astron. Union Circular 150, 3–14. https://doi.org/10.1017/S0252921100501171.

Grün, E., Zook, H., Fechtig, H., Giese, R., May 1985. Collisional balance of the meteoritic complex. Icarus 62, 244–272, 62:244–272, 1985, 0019–1035.

Grün, E., Srama, R., Krüger, H., Kempf, S., Dikarev, V., Helfert, S., Moragas-Klostermeyer, G., 2002. Kuiper prize lecture: dust astronomy. Icarus 174, 1–14. https://doi.org/10.1016/j.icarus.2004.09.010. Mar. 2005.

Horányi, M., 1996. Charged dust dynamics in the solar system. Annu. Rev. Astron. Astrophys. 34 (1), 383–418. https://doi.org/10.1146/annurev.astro.34.1.383.

Kempf, S., Altobelli, N., Briois, C., Cassidy, T., Grün, E., Horanyi, M., Postberg, F., Schmidt, J., Shasharina, S., Srama, R., Sternovsky, Z., Feb. 2014. Compositional mapping of Europa's surface with a dust mass spectrometer. LPI Contrib. 1774, 4052.

Khurana, K.K., Kivelson, M.G., Stevenson, D.J., Schubert, G., Russell, C.T., Walker, R.J., Polanskey, C., 1998. Induced magnetic fields as evidence for subsurface oceans in Europa and Callisto. Nature 395 (6704), 777–780. https://doi.org/10.1038/27394.

Kivelson, M.G., Khurana, K.K., Russell, C.T., Volwerk, M., Walker, R.J., Zimmer, C., 2000. Galileo magnetometer measurements: a stronger case for a subsurface ocean at Europa. Science 289 (5483), 1340–1343. https://doi.org/10.1126/science.289.5483.1340, 0036–8075. https://science.sciencemag.org/content/289/5483/1340.

Koschny, D., Grün, E., Dec. 2001a. Impacts into ice-silicate mixtures: ejecta mass and size distributions. Icarus 154, 402–411. https://doi.org/10.1006/icar.2001.6708.

Koschny, D., Grün, E., Dec. 2001b. Impacts into ice-silicate mixtures: crater morphologies, volumes, depth-to-diameter ratios, and yield. Icarus 154 (2), 391–401. https://doi.org/10.1006/icar.2001.6707.

Krivov, A.V., Mann, I., Krivova, N.A., Oct. 2000. Size distributions of dust in circumstellar debris discs. Astron. Astrophys. 362, 1127–1137.

Krivov, A.V., Sremčević, M., Spahn, F., Dikarev, V.V., Kholshevnikov, K.V., Mar. 2003. Impact-generated dust clouds around planetary satellites: spherically symmetric case. Planet. Space Sci. 51, 251–269.

Krüger, H., Krivov, A.V., Grün, E., Dec. 2000. A dust cloud of Ganymede maintained by hypervelocity impacts of interplanetary micrometeoroids. Planet. Space Sci. 48, 1457–1471.

Krüger, H., Krivov, A.V., Sremčević, M., Grün, E., July 2003. Impact-generated dust clouds surrounding the Galilean moons. Icarus 164, 170–187. https://doi.org/10.1016/S0019-1035(03)00127-1.

Lam, T., Buffington, B., Campagnola, S., 2018. A robust mission tour for NASA's planned Europa Clipper mission. In: 2018 Space Flight Mechanics Meeting. AIAA SciTech Forum. https://doi.org/10.2514/6.2018-0202. https://arc.aiaa.org/doi/abs/10.2514/6.2018-0202.

McCord, T.B., Hansen, G.B., Matson, D.L., Johnson, T.V., Crowley, J.K., Fanale, F.P., Carlson, R.W., Smythe, W.D., Martin, P.D., Hibbitts, C.A., Granahan, J.C., Ocampo, A., 1999. Hydrated salt minerals on Europa's surface from the Galileo near-infrared mapping spectrometer (NIMS) investigation. J. Geophys. Res.: Planets 104 (E5), 11827–11851. https://doi.org/10.1029/1999JE900005. https://agupubs.onlinelibrary.wiley.com/doi/abs/10.1029/1999JE900005.

McCord, T.B., Hansen, G.B., Hibbitts, C.A., 2001. Hydrated salt minerals on Ganymede's surface: evidence of an ocean below. Science 292 (5521), 1523–1525. https://doi.org/10.1126/science.1059916, 0036–8075. https://science.sciencemag.org/content/292/5521/1523.

Mével, L., Mercier, E., 2007. Large-scale doming on europa: a model of formation of Thera Macula. Planet. Space Sci. 55 (7), 915–927. https://doi.org/10.1016/j.pss.2006.12.001, 0032–0633. http://www.sciencedirect.com/science/article/pii/S0032063306003436.

O'Brien, D.P., Geissler, P., Greenberg, R., 2002. A melt-through model for chaos formation on Europa. Icarus 156 (1), 152–161. https://doi.org/10.1006/icar.2001.6777, 0019–1035. http://www.sciencedirect.com/science/article/pii/S0019103501967776.

Pappalardo, R.T., Sullivan, R.J., 1996. Evidence for separation across a gray band on Europa. Icarus 123 (2), 557–567. https://doi.org/10.1006/icar.1996.0178, 0019–1035. http://www.sciencedirect.com/science/article/pii/S0019103596901785.

Pappalardo, R.T., Head, J.W., Greeley, R., Sullivan, R.J., Pilcher, C., Schubert, G., Moore, W.B., Carr, M.H., Moore, J.M., Belton, M.J.S., Goldsby, D.L., 1998. Geological evidence for solid-state convection in Europa's ice shell. Nature 391 (6665), 365–368. https://doi.org/10.1038/34862.

Poppe, A.R., 2016. An improved model for interplanetary dust fluxes in the outer solar system. Icarus 264, 369–386. https://doi.org/10.1016/j.icarus.2015.10.001, 0019–1035. https://www.sciencedirect.com/science/article/pii/S0019103515004674.

Postberg, F., Kempf, S., Hillier, J., Srama, R., Green, S., McBride, N., Grün, E., 2008. The E-ring in the vicinity of Enceladus: ii. probing the moon's interior—the composition of E-ring particles. Icarus 193 (2), 438–454. https://doi.org/10.1016/j.icarus.2007.09.001, 0019–1035. https://www.sciencedirect.com/science/article/pii/S0019103507003867 (Saturn's Icy Satellites from Cassini).

Postberg, F., Kempf, S., Schmidt, J., Brilliantov, N., Beinsen, A., Abel, B., Buck, U., Srama, R., June 2009. Sodium salts in E-ring ice grains from an ocean below the surface of Enceladus. Nature 459, 1098–1101. https://doi.org/10.1038/nature08046.

Postberg, F., Grün, E., Horanyi, M., Kempf, S., Krüger, H., Schmidt, J., Spahn, F., Srama, R., Sternovsky, Z., Trieloff, M., 2011. Compositional mapping of planetary moons by mass spectrometry of dust ejecta. Planet. Space Sci. 59 (14), 1815–1825. https://doi.org/10.1016/j.pss.2011.05.001, 0032–0633. http://www.sciencedirect.com/science/article/pii/S0032063311001553 (Lunar Dust, Atmosphere and Plasma: The Next Steps).

Postberg, F., Khawaja, N., Abel, B., Choblet, G., Glein, C.R., Gudipati, M.S., Henderson, B.L., Hsu, H.-W., Kempf, S., Klenner, F., Moragas-Klostermeyer, G., Magee, B., Nölle, L., Perry, M., Reviol, R., Schmidt, J., Srama, R., Stolz, F., Tobie, G., Trieloff, M., Waite, J.H., jun 2018. Macromolecular organic compounds from the depths of Enceladus. Nature 558 (7711), 564–568. https://doi.org/10.1038/s41586-018-0246-4.

Sachse, M., Schmidt, J., Kempf, S., Spahn, F., 2015. Correlation between speed and size for ejecta from hypervelocity impacts. J. Geophys. Res.: Planets 120 (11), 1847–1858. https://doi.org/10.1002/2015JE004844. https://agupubs.onlinelibrary.wiley.com/doi/abs/10.1002/2015JE004844.

Schenk, P.M., 1995. The geology of Callisto. J. Geophys. Res.: Planets 100 (E9), 19023–19040. https://doi.org/10.1029/95JE01855. https://agupubs.onlinelibrary.wiley.com/doi/abs/10.1029/95JE01855.

Spahn, F., Schmidt, J., Albers, N., Kempf, S., Krivov, A.V., Makuch, M., Schmidt, J., Seiß, M., Sremčević, M., Aug. 2006a. E ring dust sources: implications from Cassini's dust measurements. Planet. Space Sci. 54, 1024–1032. https://doi.org/10.1016/j.pss.2006.05.022.

Spahn, F., Schmidt, J., Albers, N., Hörning, M., Makuch, M., Seiß, M., Kempf, S., Srama, R., Dikarev, V., Helfert, S., Moragas-Klostermeyer, G., Krivov, A.V., Sremčević, M., Tuzzolino, A.J., Economou, T., Grün, E., Mar. 2006b. Cassini dust measurements at enceladus and implications for the origin of the E ring. Science 311, 1416–1418. https://doi.org/10.1126/science.1121375.

Srama, R., Ahrens, T.J., Altobelli, N., Auer, S., Bradley, J.G., Burton, M., Dikarev, V.V., Economou, T., Fechtig, H., Görlich, M., Grande, M., Graps, A., Grün, E., Havnes, O., Helfert, S., Horanyi, M., Igenbergs, E., Jessberger, E.K., Johnson, T.V., Kempf, S., Krivov, A.V., Krüger, H., Mocker-Ahlreep, A., Moragas-Klostermeyer, G., Lamy, P., Landgraf, M., Linkert, D., Linkert, G., Lura, F., McDonnell, J.A.M., Möhlmann, D., Morfill, G.E., Müller, M., Roy, M., Schäfer, G., Schlotzhauer, G., Schwehm, G.H., Spahn, F., Stübig, M., Svestka, J., Tschernjawski, V., Tuzzolino, A.J., Wäsch, R., Zook, H.A., Sept. 2004. The cassini cosmic dust analyzer. Space Sci. Rev. 114, 465–518. https://doi.org/10.1007/s11214-004-1435-z.

Srama, R., Woiwode, W., Postberg, F., Armes, S.P., Fujii, S., Dupin, D., Ormond-Prout, J., Sternovsky, Z., Kempf, S., Moragas-Klostermeyer, G., Mocker, A., Grün, E., 2009. Mass spectrometry of hyper-velocity impacts of organic micrograins. Rapid Commun. Mass Spectrom. 23 (24), 3895–3906. https://doi.org/10.1002/rcm.4318. https://analyticalsciencejournals.onlinelibrary.wiley.com/doi/abs/10.1002/rcm.4318.

Sremčević, M., Krivov, A.V., Spahn, F., June 2003. Impact-generated dust clouds around planetary satellites: asymmetry effects. Planet. Space Sci. 51, 455–471.

Sremčević, M., Krivov, A.V., Krüger, H., Spahn, F., May 2005. Impact-generated dust clouds around planetary satellites: model versus Galileo data. Planet. Space Sci. 53, 625–641. https://doi.org/10.1016/j.pss.2004.10.001.

Thomopoulos, N.T., 2013. Essentials of Monte Carlo Simulation. Springer, New York. https://doi.org/10.1007/978-1-4614-6022-0.